

Determination of Electrode Balancing in Multilayer Pouch Cells Through Tracking and Tracing in Lithium-Ion Battery Production

Alessandro Sommer,^{*[a]} Jannis Wachter,^[a] Sophie Grabmann,^[a] and Rüdiger Daub^[a, b]

Manufacturing lithium-ion batteries is a complex procedure with interconnected process steps. Unknown interdependencies lead to production deviations, which, in combination with expensive materials, result in costly rejects. To gain better insight into the processes, tracking and tracing systems are increasingly being established in battery cell production. This improves the database and enhances transparency, as quality-critical production data is already recorded during electrode production and specifically assigned to individual intermediate products. The data assignment aids in characterizing intermediate products properties to identify correlations and defects. An important parameter is the balancing from cathode to anode,

which has a crucial influence on cell performance. Therefore, this paper demonstrates the determination of the balancing between all electrode layers in a lithium-ion pouch cell using a traceability system. The traceable areal mass loading was determined for each electrode sheet. After the stacking process, the opposing electrode areal mass loadings of the cathodes and anodes were used to calculate the electrode balancing. Subsequently, their influence on the cycling performance of the cells was investigated. Battery cells with areal mass loadings within the permissible tolerances showed no abnormalities, whereas cells with production fluctuations exhibited rapid ageing.

Introduction

The Intergovernmental Panel on Climate Change has reported a slower but ongoing world-wide increase in anthropogenic greenhouse gas emissions in their sixth assessment report in 2023.^[1] The transport and energy sectors demonstrate that reducing emissions from these areas can significantly contribute to the reduction of greenhouse gases.^[2] The transition within the transport sector to battery electric vehicles has led to an increasing global market for batteries.^[3] This demand had the effect of rapid innovations which resulted in higher energy density and lower costs for batteries in recent years.^[4] However, the battery pack still accounts for the largest share in final product costs of electric vehicles.^[5] Lithium-ion battery (LIB) manufacturing is characterized by a long process chain with high and unknown interdependencies.^[6] From this arise manufacturing inaccuracies and defects, which, in combination with high material costs, lead to costly scrap expenses.^[7] To better understand the complex relationships in battery cell

production, data-driven approaches are increasingly being used to build a deeper understanding of cause-effect relationships.^[8–10] By collecting and evaluating production data, these approaches are used to get a deeper understanding and control the production processes.^[11–13] In addition the use of data mining methods is reported in a lithium-ion cell production line to analyze and improve production processes. The CRISP-DM methodology is used to determine process dependencies, key factors for product quality and the prediction of product quality before the complex formation and ageing process.^[14] Another use case for data-driven approaches is the implementation of virtual quality gates.^[15] By introducing decision points, measurement steps can be combined to reduce the effort needed for quality control and to consolidate information on important quality parameters of intermediate products.^[16,17]

To enable these data-driven approaches, the use of traceability systems is recommended.^[18] This is intended to create a consistent data foundation that is needed for building understanding within the process chain.^[19] They provide consistent data records and additionally link the determined quality data to the respective intermediate products.^[19] With the help of improved transparency, cause-and-effect relationships are intended to be uncovered, and corresponding measures for quality assurance derived.^[16] Traceability concepts are already successfully used by tracking and tracing relevant process- and product data in other industries such as logistics,^[20] food,^[21] and pharmaceuticals,^[22] but are currently not described in literature for an industrial scale in LIB production. For the implementation of a traceability system, a traceable resource unit (TRU) is needed. The TRU represents the smallest traceable unit of intermediate products and can be connected and characterized

[a] A. Sommer, J. Wachter, S. Grabmann, Prof. Dr. Ing. R. Daub
Technical University of Munich
TUM School of Engineering and Design, Institute for Machine Tools and Industrial Management (iwb)
Boltzmannstr. 15, Garching 85748 (Germany)
E-mail: Alessandro.sommer@iwb.tum.de

[b] Prof. Dr. Ing. R. Daub
Fraunhofer Institute for Casting, Composite and Processing Technology (IGCV)
Am Technologiezentrum 10, 86159 Augsburg (Germany)

© 2024 The Authors. Batteries & Supercaps published by Wiley-VCH GmbH.
This is an open access article under the terms of the Creative Commons Attribution License, which permits use, distribution and reproduction in any medium, provided the original work is properly cited.

with production data.^[18] For the detection of the TRU, an identification method is required, which can be implemented in the form of a physical marking. In the case of battery production, markings are already used on the cell casings for the traceability of manufactured cells.^[23,24] However, to make quality-relevant production data traceable already during production, the identification of the intermediate products of an individual cell is required. It has been reported that markings are already applied to individual electrodes for this purpose.^[25–27] This enables, for example, errors in the coating to be traced back to individual electrode sections.^[28] The markings are used to segment continuous processes and to assign production data to individual electrode sheets.^[29] Furthermore, it was demonstrated that a marking-based traceability system was integrated along the entire process chain, and production-relevant data could be assigned to all intermediate products.^[30] In summary, in literature is described that data-driven approaches can benefit from the improved data foundation provided using traceability systems. Furthermore, it has been reported that the implementation of a comprehensive traceability system, from mixing to the formation process of battery cell production, has already been achieved. However, no application has yet been demonstrated in which the data from a traceability system has been used for quality-relevant purposes.

The aim of this work was to reveal a data-based use case for quality-relevant analysis in battery cell production through tracking and tracing. This was demonstrated using the production of large-format pouch cells in a pilot line, in which a comprehensive traceability system was integrated. In this case, the traced areal mass loadings of each individual electrode sheet were used to determine the resulting balancing between the individual electrode layers. This so-called N/P ratio has a crucial impact on the electrochemical performance of battery cells^[31,32] and has been previously studied.^[33] Subsequently, the effects of different balanced electrode stacks on cycling performance were examined and visually inspected by post-mortem analysis.

Experimental

General Pouch Cell Production

Multilayer pouch cells were manufactured on the pilot line of the Institute for Machine Tools and Industrial Management (*iwb*) at the Technical University of Munich. This production line was successfully used for the manufacturing of previous battery cells.^[34–38] The production is divided into the electrode manufacturing and the cell assembly. The electrode manufacturing, consisting of mixing, coating, drying, and calendering, took place in a clean room class 1000/ISO 6. Cell assembly, consisting of confectioning, stacking, contacting, packaging, vacuum drying, filling, and formation was done in a drying room with a dew point of -45°C . Parallel to the manufacturing process, all available production data was recorded using the established traceability system. More information regarding the traceability system is provided in SOMMER et al.^[30] The three TRUs defined in this LIB production at the *iwb* were the slurry, the electrode, and the cell. The production data from electrode

manufacturing was assigned on an electrode sheet-specific basis, and the data from cell assembly and finalization was assigned to the produced cell stacks or battery cells accordingly. In the context of this publication, only areal mass loading is considered as a quality parameter from the traceability system. From this, the resulting area capacity can be calculated, and consequently, the balance between the respective cathode and anode pairings. The calculated N/P ratio is based on this parameter.

Mixing

The components for the cathode slurry were mixed with N-Methyl-2-pyrrolidone (NMP, Sigma-Aldrich, USA) and the anode slurry with water at ambient pressure and temperature. The cathode slurry consisted of 95.5 wt% lithium nickel manganese cobalt oxide (NMC622, BASF, Germany) with a specific capacity of approx. 163 mAh g^{-1} , 2.25 wt% conductive carbon (C65, Imerys, Switzerland), 1.5 wt% polyvinylidene fluoride (PVDF, Solvay, Belgium), and 0.75 wt% graphite (SFG6L, Imerys, Switzerland). The anode slurry contained 94 wt% graphite (SMGA5, Hitachi, Japan) with approx. 355 mAh g^{-1} , 3 wt% styrene-butadiene rubber (SBR, ZEON, Japan), 2 wt% carboxymethyl cellulose (CMC, Sigma-Aldrich, USA), and 1 wt% conductive carbon (C65, Imerys, Switzerland). Regarding the traceability system, no special marking was used for the slurry since it was immediately processed after the production. All production data from the produced slurries were assigned to the respective electrode coils.

Coating and Drying

Doctor blade coating was performed in an industrial roll-to-roll coating machine (BC50, Coatema GmbH, Germany) equipped with three drying stages. Inline ultrasound systems (MeSys wet CFS400-USMX200 and MeSys dry OF400-USMX200, MeSys GmbH, Germany) were used to measure the wet film mass loading directly after coating, as well as the dry film areal mass loading. The cathode slurry was coated double-sided onto an aluminum current collector foil (nominal thickness of $15 \mu\text{m}$, AA1100/H19, Speira, Germany) at a speed of 0.8 m min^{-1} . The three dryer stages were set to 70°C , 75°C , and 80°C . The coating of one side had a target areal mass loading of 16.76 mg cm^{-2} . The anode slurry was coated double-sided onto a copper current collector foil (nominal thickness of $10 \mu\text{m}$; Se-Cu58, Carl Schlenk AG, Germany) at a speed of 0.5 m min^{-1} . The three dryer stages were set to 40°C , 50°C , and 55°C . The coating of one side had a target areal mass loading of 9.79 mg cm^{-2} . The electrode coil served as the central unit in the coating and drying process. However, since multiple electrodes were cut from a single coil to assemble a cell, it became necessary to initiate data tracking at the electrode-specific level early in the process. Consequently, a marking unit was integrated into the coating and drying procedure, employing an ytterbium fiber laser (FOBA Y.0300-xs, ALLTEC GmbH, Germany) for applying Data Matrix codes (DMCs). Figure 1a depicts the coating and drying machine utilized in production, providing detailed explanations of the components, and measuring points. The travel path, along with the direction of travel, is delineated in red. The implementation of the marking laser, along with laser safety housing, is illustrated in Figure 1b. For the electrode identification, two-dimensional DMC with 16×16 modules according to ISO/IEC 16022:2006 were used. The marking frequency was chosen to enable the identification of each individual electrode sheet to be cut from the coils in subsequent production steps. For DMC spacing, the width of the electrodes, with a 5 mm margin, was selected, resulting in marking spacing of 81 mm for the anodes and 78 mm for the cathodes. Since the laser was positioned at the end of the process line due to

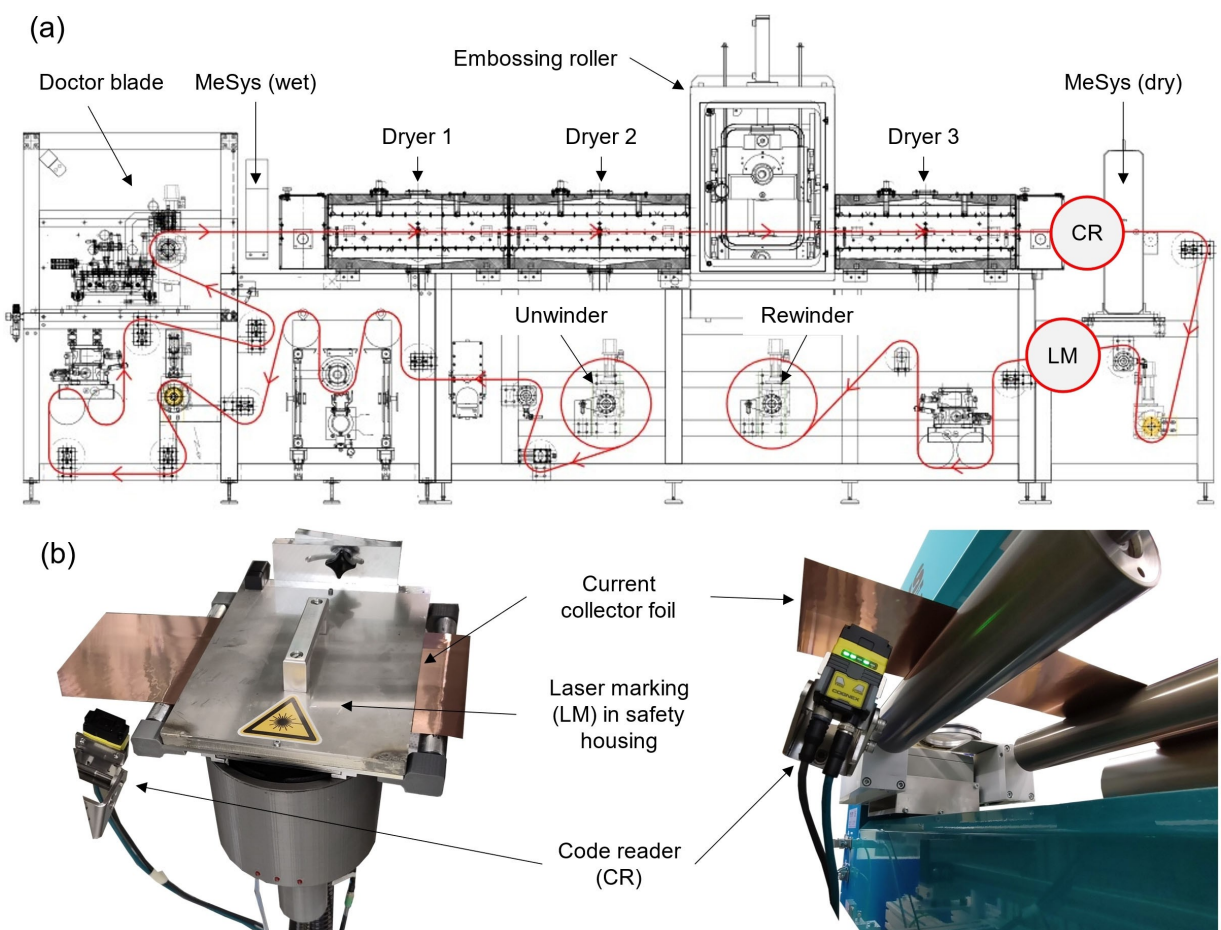


Figure 1. The technical drawing of the coating and drying machine is shown in (a), including the explanations of the components and measurement points. In addition, the travel path of the current collector foil is shown in red with arrows indicating the direction of travel. In (b), the pictures illustrate the integration of the laser marking unit, complete with safety housing and code reader, as well as the integration of a second code reader positioned between the third dryer and the areal mass loading measurement system, referred to as MeSys (dry).

space constraints, immediate reading of the DMCs with a code reader (DataMan280, Cognex, USA) was necessary before the coil was rolled up. Due to the double-sided coating and thus the second pass of the coil through the system, a second code reader was necessary. This code reader detected the DMCs on the opposite side to assign the corresponding production parameters for the second coating process. With the help of the traceability system, the recorded areal mass loading from the coating process could be unequivocally assigned to individual subsequent electrode sheets on a side-specific basis.

Calendering

A calender (EA 102, Coatema GmbH, Germany) with a roll diameter of 400 mm and a maximum line load of 1000 N mm^{-1} was used to compact the electrodes. For the measurement of the thickness of the electrodes before and after calendering, a tactile dial gauge (40 EWRI, Mahr GmbH, Germany) was used. The cathodes were compacted from 43% ($\rho_{\text{Coating}} = 2.53 \text{ g cm}^{-3}$) to 30% ($\rho_{\text{Coating}} = 3.11 \text{ g cm}^{-3}$) porosity with a roller temperature of 90°C. The total cathode thicknesses (including two cathode coatings and one 15 µm aluminum foil) were compressed from 155 µm to 122 µm. The anodes were compacted from 41% ($\rho_{\text{Coating}} = 1.25 \text{ g cm}^{-3}$) to 30% ($\rho_{\text{Coating}} = 1.50 \text{ g cm}^{-3}$) porosity with a roller temperature of 25°C. The total anode thicknesses (including two anode coatings

and one 10 µm copper foil) were compressed from 216 µm to 141 µm. Figure 2a shows the drawing of the calender including the path and direction of travel of the electrode coil in red. A third code reader was implemented after the calender rollers that allowed the identification of the DMCs during the calendering process and consequently for the assignment of the calender production data, shown in Figure 2b.

Electrode Separation

Electrode coils were separated with a laser cutting system (HP-02-30-500-100-LT, IPG Photonics, USA). The pulsed laser radiation had a wavelength of 1064 nm, a pulse width of 30 ns, and a pulse frequency of 500 kHz. The cut electrode sheets for the anodes have a size of 7904 mm^2 with a remaining uncoated current collector foil. The cut electrode sheets for the cathode had a size of 7373 mm^2 with the same size of uncoated current collector foil for current conduction. In Figure 3, the cut electrodes and dimensioned outlines are shown.

The precise dimensions of the cut electrode format is described by KRIEGLER et al.^[36]

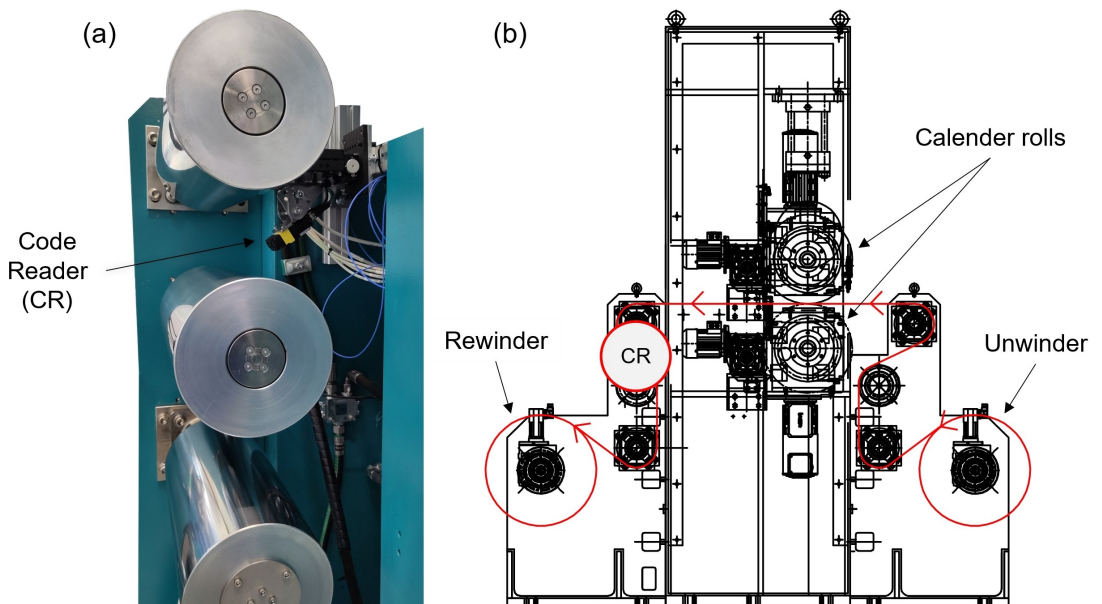


Figure 2. The technical drawing of the calender including the travel path and the direction of the electrode coil are shown in red with arrows in (a). In (b) the integration of the code reader is shown. The main measuring point of the calender parameters is the line contact between the two calender rolls.

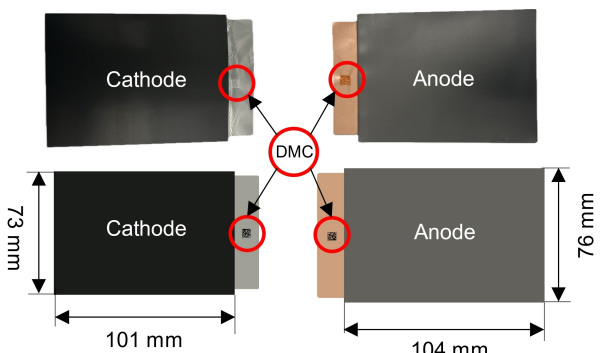


Figure 3. Pictures of the cut cathodes and anodes are shown above, below are the corresponding dimensioned outlines of the electrodes. The applied DMC is indicated in red.

Cell Stacking

The stacking system was developed in cooperation with Manz Automation AG.^[39] The cell stacks were z-folded with a polymer separator (C2325, Celgard LLC, USA). The electrode stacks consisted of six double-sided coated anodes and five double-sided coated cathodes. The stacks were wrapped with the ending of the separator and fixed with a tape to guarantee mechanical stability. For the investigation, in total six pouch cells were manufactured in two different batches. Batch 1 consisted of three reference cells. The three cells contained only electrodes with areal mass loadings within the permissible coating tolerance of 5%. Batch 2 included 3 manipulated cells where electrodes with intentionally excessive areal mass loading were added during the stacking process. All electrodes, except for one cathode sheet, were within the coating tolerance. This particular cathode sheet exceeded the tolerance, with approximately 20% excess loading. For the traceability system, two further code readers were integrated into the stacking system for both cathode and anode sheets. These readers identify the applied DMCs on the electrode sheets during the stacking process and associate them, along with their order, with the constructed

cell stacks. In Figure 4a, the z-folding machine used for stacking electrodes is depicted. The cuts on the right and left of Figure 4b display the cathode and anode magazines containing loaded electrode sheets marked with DMCs, along with the two code readers.

For all following process steps of cell assembly, the used machine parameters and captured product characteristics were recorded using a self-programmed digital input and a unique marking on the cell stack or cells and assigned to the intermediate products.

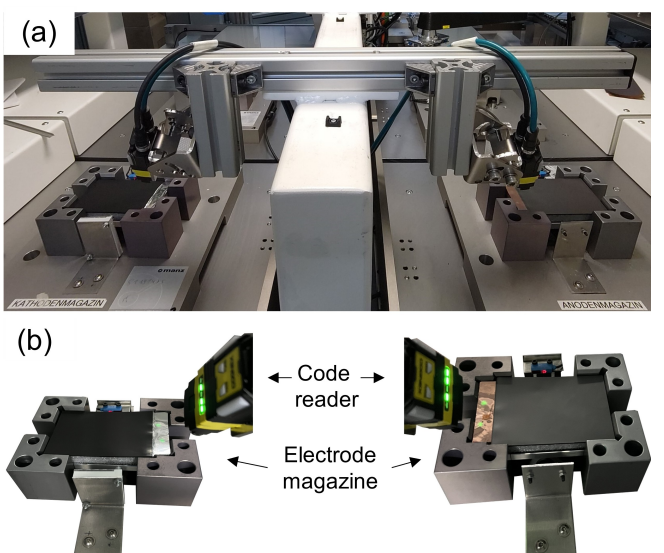


Figure 4. In (a), the implementation of the code readers in the z-folding machine is shown. In (b), the left and right insets show the detection of the electrode DMCs in the cathode and anode magazines.

Determination of the Electrode Balancing

With the help of the installed traceability system, the electrode balancing was determined. Through the segmentation of the electrode manufacturing, the recorded loading values were assigned to the individual electrode sheets. Due to the consecutive coating of the first and second sides, the respective areal mass loadings of both sides could be clearly determined. Based on the assigned areal mass loading, the areal capacity C_{areal} of the respective side of each electrode sheet was calculated by using the measured areal mass loading of the respective coating side $g_{E,Coating}$, the ratio of active material $P_{E,AM}$ and the specific capacity $c_{E,AM,spec}$ of the electrode. The calculation is presented in Equation 1.

$$C_{areal} = g_{E,Coating} * P_{E,AM} * c_{E,AM,spec} \quad (1)$$

Furthermore, through the code readers in the z-folding machine, the position in the cell stack and the orientation of each electrode sheet was known. Subsequently, the specific capacity ratio of the negative electrode (anode) to the positive electrode (cathode) N/P between each layer was determined from the opposite areal capacities C_{areal} . It was calculated by dividing the specific areal capacity of the anode by the specific areal capacity of the cathode.^[40,41] This was done for each opposing electrode layer in every cell.

Contacting

Current collector foils and the cell tabs were contacted by an ultrasonic welding machine (Branson Ultraweld L20, Emerson Electric Co., USA). For the cathodes, the current collector foils were initially contacted with an amplitude of 13 µm, a frequency of 20 kHz, a welding energy of 90 J, and a clamping force of 97 kPa. The anodes were contacted with an amplitude of 25 µm, a frequency of 20 kHz, a welding energy of 450 J, and a clamping force of 172 kHz. The cell tabs were each attached with the settings of the cathode and anode sides, respectively. The weld seams had a size of 68 mm · 3 mm on both sides.

Packaging

The cell stacks were packed into a flexible deep-drawn pouch bag. Three sides were sealed with a sealing machine (HH – 4424 003, Harro Hoefliger GmbH, Germany). The parameters for the sealing bars were 6 s sealing time, 220 °C sealing temperature, 3.5 bar sealing pressure, and a residence time of 10 s. One side was left open for the electrolyte filling.

Electrolyte Filling

All pouch cells were inserted into a glove box via a vacuum lock for 12 h at 60 °C. The glove box contained a nitrogen atmosphere to prevent water contamination. The cell batches were filled by hand using a pipette (EP Research plus G, Eppendorf GmbH, Germany) with 5.6 ml of electrolyte (LP572, BASF, Germany) containing ethylene carbonate (EC) and ethyl methyl carbonate (EMC) at a ratio of 3:7 by weight as solvents with 1 M lithium-hexafluorophosphate (LiPF6) and 2 wt% vinylene carbonate. Before sealing the filled pouch cells, each cell was inserted into a vacuum and sealing system, where chamber pressure was reduced to 200 mbar. After two hours of wetting, the formation was started.

Formation

All cells went through a formation procedure consisting of three charge and discharge cycles at a C-Rate of C/10. Charging was conducted in constant current (CC) operation in the first two cycles and in constant current/constant voltage (CCCV) mode in the third cycle with a cutoff current at C/20. Discharging was performed in a CC procedure within a voltage range of 4.2 V to 2.9 V at a constant temperature of 25 °C. The discharge capacity of the third formation cycle was defined as the nominal capacity of the cells. Parallel to the formation process, using the tracking and tracing system, the theoretical capacity of the cells C_{cell} was determined from the traced areal mass loading of the cathodes and compared with the measured capacity of the battery cells from both batches. Therefore, the already calculated areal capacity C_{areal} was multiplied by the area of the cathode surface A_C , and the sum of all ten cathode coatings i in a cell was determined, as shown in Equation 2.

$$C_{cell} = \sum_{i=1}^{10} C_{areal,i} \cdot A_C \quad (2)$$

The exact description of the calculation of the areal mass loading can be found in SOMMER et al.^[30]

Cycle Life Testing

The pouch cells were cycled with equal test conditions to monitor their state of health (SOH) during cycle life testing. Hereby, the cells were cycled with 1 C CCCV for charging and 1 C CC for discharging between 2.9 and 4.2 V at 25 °C with a pressure of 2 bar applied by the cell carriers. Additionally, a checkup was done every 50 cycles. During checkup, two cycles were carried out with 0.1 C CCCV for charging and 0.1 C CC for discharging. The life cycle tests were carried out for 1002 cycles including the checkups.

Post-Mortem Analysis

Following the cycle life testing, the cells were opened within a specially designed glove box for post-mortem analysis, developed in collaboration with MBraun GmbH. In this process, the cells were opened, and the respective cathodes, anodes, and separator layers were successively unfolded from the cell stack. Detailed images were captured of the cell components. Furthermore, recordings of the markings of each cathode and anode sheet were made. The setup for the post-mortem analysis was verified and successfully used for previous cell teardown studies of battery cells.^[23,24,42] The opening procedure took place in an argon environment with H₂O and O₂ concentration below 0.1 ppm.

For further examination of the electrode surface, a scanning electron microscope (SEM, IT-200, JEOL, Japan) operating at 15 kV was used. For this purpose, the electrodes were cut, and a magnification of 350 was selected for lateral views and 1800 for top views.

Results and Discussion

The areal mass loading of the produced and cut electrodes were determined by using the traceability system. As the electrodes were coated on both sides, the areal mass loadings of the respective side and the current collector foils were determined. In the calculation of the coating loading, the areal mass loading of the current collector foils was subtracted. It

was assumed that the areal mass loading of the foils was constant over the entire coil. For the aluminum foil, a value of 4.2 mg cm^{-2} was measured, and for the copper foil 9.3 mg cm^{-2} . In Figure 5, the areal mass loadings off all installed electrode sheets from the reference cells and the manipulated cells are shown. The reference cells are abbreviated as Ref, the manipulated cells as Man. The respective cathodes are abbreviated as C, and the anodes as A. The number after the electrode C or A indicates the respective electrode in the correct order of the cell stack.

The single-sided areal mass loading of all installed anode sheets is within the tolerance limits close to the target value of 9.79 mg cm^{-2} . For the cathodes in the reference cells, all electrode sheets are within the tolerance limits close to the target value of 16.76 mg cm^{-2} . In the manipulated cells, all electrode sheets, except for the C3 cathode sheets, were within tolerance. The traced areal mass loading of the intentionally manually introduced C3 cathode sheets was increased by approximately 20%. The tolerance range and variations of the areal mass loading can fundamentally be attributed to the use of doctor blade coating. This method is not preferred for large-scale industrial applications due to the tendency to exhibit greater deviations.^[43] Slot die coating is recommended to achieve more precise results.^[44] For the used research production line, however, slot die coating is preferred due to the lower material consumption. Furthermore, the coating of the first and second side were carried out consecutively. When measuring the areal mass loading of the second side, the current collector foil, which can be considered constant, and the first coating side were measured together. This means that the measurement of the second coating side is influenced by the deviations of the first side. Virtual cell stacks were created from the assigned production data of the installed electrode sheets. For this purpose, the cell stack was digitally represented and assigned with the specific areal mass loading. Through the code readers in the z-folding machine, the orientation and position of each individual electrode sheet in every cell stack was determined. Subsequently, the areal mass loadings were used

to calculate the respective areal capacity of each individual electrode sheet. For this calculation, the specific capacity of the active materials, the active material fraction, and the traced areal mass loading were used, according to SOMMER et al.^[30] Exemplarily, Figure 6 illustrates the traced areal mass loadings, calculated specific areal capacities, and N/P ratios between the individual electrode sheets of the cells Ref. [1] in (a) and Man 1 in (b). The schematic representation in Figure 6 is a possible illustration of virtual representations of the cells. This serves to illustrate production fluctuations and their effects on local N/P ratios. The graphical representation facilitates a visual comprehension; however, this can also be described in tabular form and through the clear electrode positions.

The cell stacks illustrated a digital representation in terms of areal mass loading, made possible only through the traceability system. The fine-grained data resolution allows assigning a specific averaged areal mass loading value to each electrode sheet. Furthermore, the digital representation was utilized to determine the local N/P ratios between individual layers. It can be observed that the local N/P ratio in cell Ref. [1] ranges between 1.167 and 1.373. The overbalancing of the anodes results in a lower energy density; however, this reduces the risk of lithium plating.^[45] The N/P ratio in cell Man 1 is comparable to cell Ref. [1], except for the two electrode pairings around electrode position 6. At this point, the overloaded cathode sheet C3 is located, causing a balancing of 0.910 and 1.001. The reduced N/P ratio at this point locally increases the risk of lithium plating and consequently decreases the cycle stability of the electrodes.^[46] In summary, the assigned data was used to calculate the electrochemical balancing of the opposing electrode layers to make an initial estimation of enhanced lithium plating.

For the formation process, the assigned areal mass loadings of the single electrode sheets were used to determine the theoretical capacity of the battery cells. The cells were formed, and the discharge capacity after the third formation cycle was defined as the initial cell capacity before cycling. The compar-

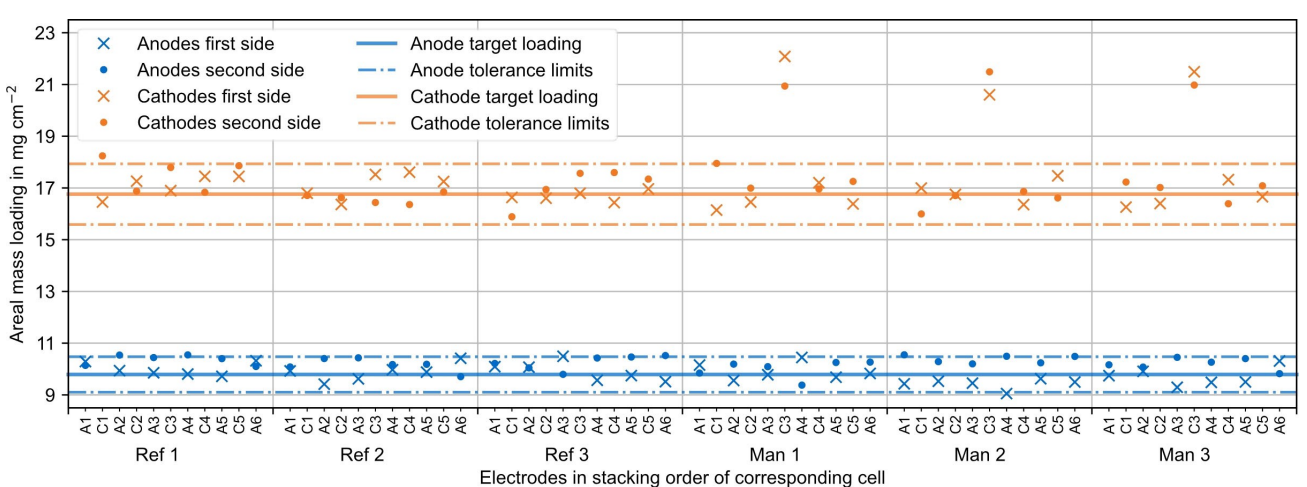


Figure 5. Areal mass loading of both sides from all used electrode sheets in the stacked cells. The respective loading of the first and second side of each electrode sheet is shown for each individual cell.

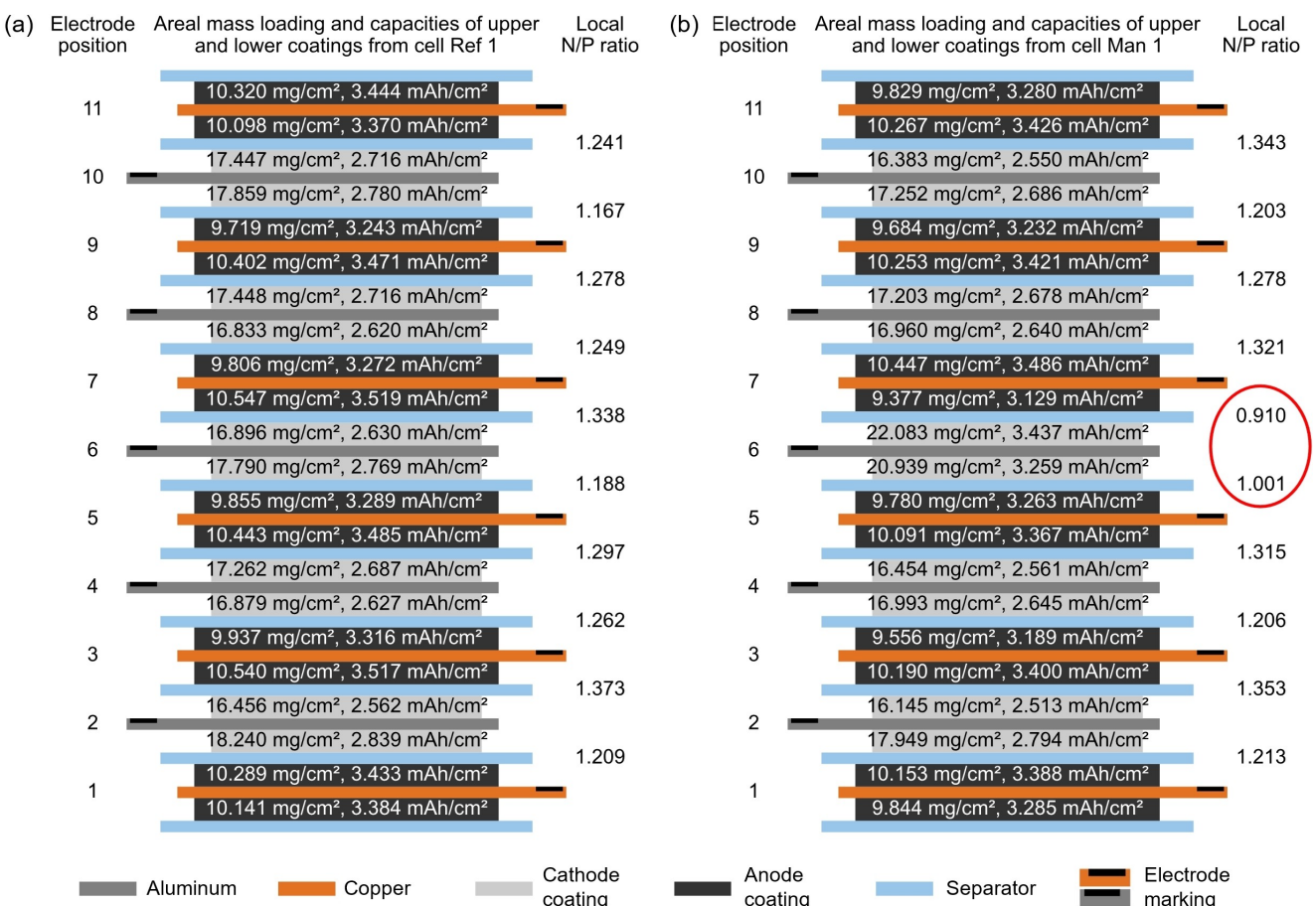


Figure 6. Schematic representation of the electrode sheet-specific areal mass loadings, calculated areal capacities, and the resulting N/P ratios for the individual layers of cell Ref. [1] from batch 1 in (a), as well as cell Man 1 from batch 2 in (b). The critical N/P ratios in cell Man 1, caused by the manually introduced overloading of cathode sheet C3, are marked in red.

ison of the calculated and measured capacities of the battery cells is shown in Figure 7.

It was observed that the reference cells had a theoretically calculated capacity of 1.953 ± 0.027 Ah and a measured capacity

of 1.955 ± 0.041 Ah. The calculated and measured capacities of the reference cells showed a high level of agreement. The manipulated cells had a theoretical capacity of 2.032 ± 0.015 Ah and a measured capacity of 2.007 ± 0.005 Ah. The manipulated cells had approximately 4% more theoretically calculated capacity compared to the reference cells. This can also be explained by the areal mass loadings as shown in Figure 5. The cathode sheets, which are excessively loaded, possess approximately 20% more capacity. As a result, a cell stack containing four cathode sheets within the tolerance range is formed, resulting in an average capacity increase on cell level of 4%. In contrast, the manipulated cells exhibited only about a 2.6% measured capacity increase. This can be explained by the fact that the increased cathode loading of the C3 cathodes, along with a constant anode loading, does not allow the added capacity to be fully utilized. This is also evident in the N/P ratio from Figure 6b, which is less than 1 indicating a capacity increase is not possible.^[47]

All manufactured battery cells underwent cycle life testing. The cycle life performance of the manufactured cells was investigated using the specific discharge capacity related to the nominal capacity from the formation. The development of the SOH is shown in Figure 8a. To further investigate the behavior

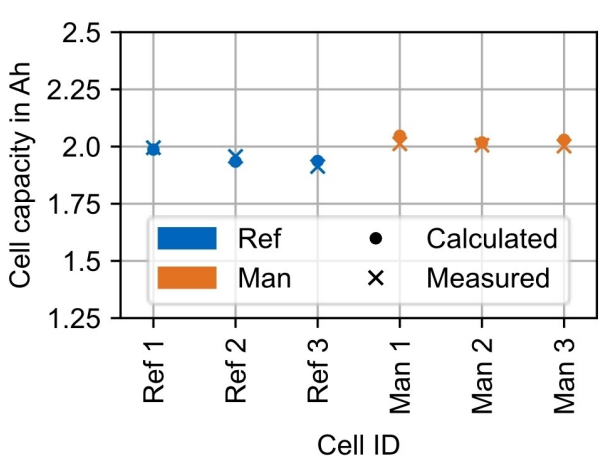


Figure 7. Comparison of the electrode sheets-based calculated and measured capacities of the produced reference and manipulated battery cells.

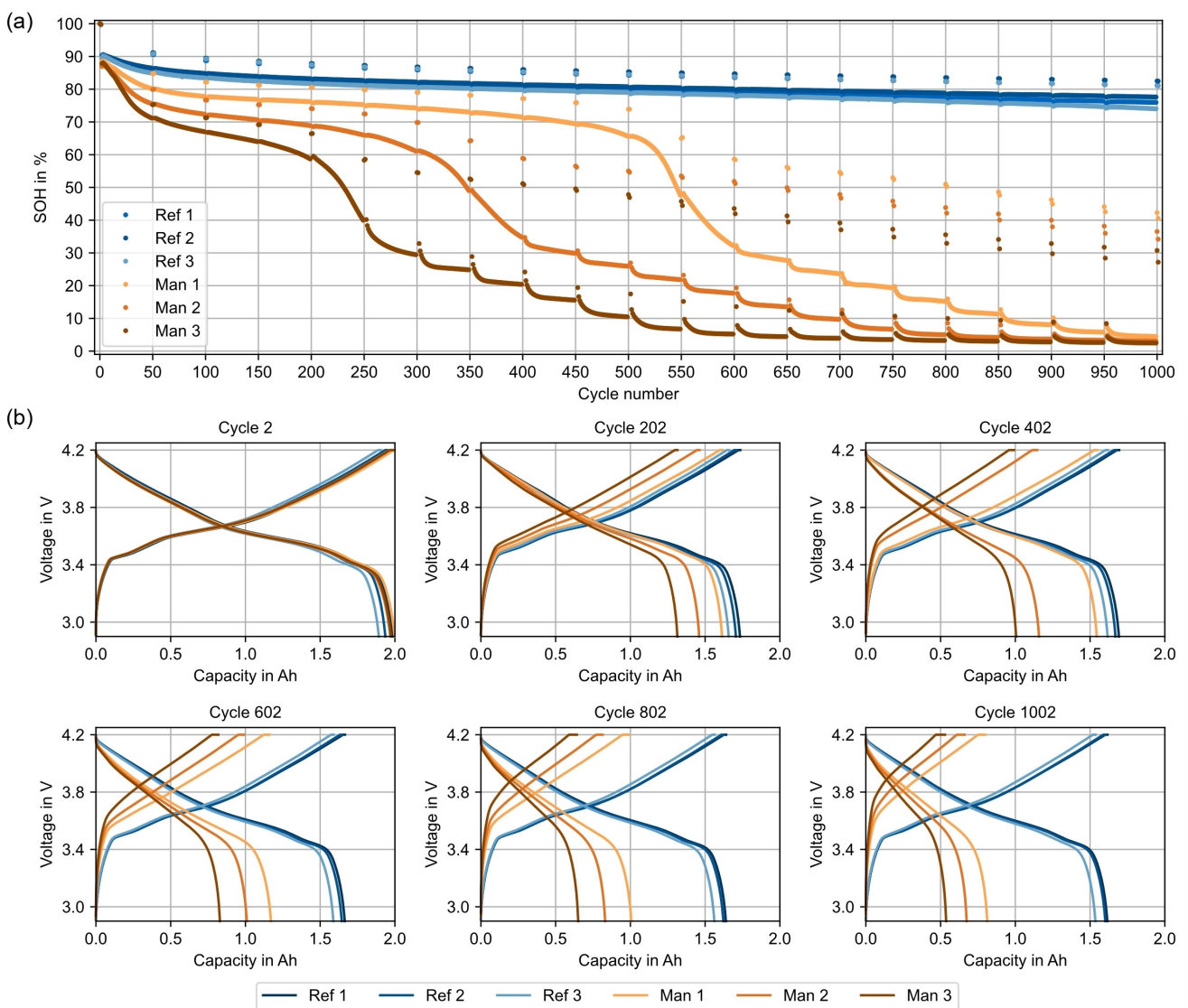


Figure 8. The normalized discharge capacities of the cycle life testing for the reference and manipulated pouch cells are shown in (a). The cell voltages during charging and discharging of every second checkup cycle as a function of the capacity are shown in (b). The results of this investigation demonstrated the influence of the inserted overloaded cathode electrode sheet within the manipulated cell batch.

of cycling aging during cycle life testing, the voltage curves of all reference and manipulated cells were examined and shown in Figure 8b. For this, the voltage curves from the second checkup cycle for all 200 cycles are shown.

The manipulated cells exhibited a more pronounced aging behavior compared to the reference cells, which is evident in the faster decrease in discharge capacity. The reference cells showed their strongest degradation behavior in the first 50 cycles. The SOH of the reference cells is approximately 90% at cycle 50 of the second checkup. Subsequently, the cells aged more slowly until the last checkup after 1002 cycles, where they had approximately 81% SOH. The reference cells showed little deviation within the cells. In comparison, the manipulated cells aged much faster. Within the first 50 cycles, the SOH of the manipulated cells in the check-up dropped to approximately 80%. This corresponded to an almost twice as fast aging

compared to the reference cells. Between cycles 50 and 200, the manipulated cells aged only slightly less and consistently compared to the initial cycles. From cycle 200, accelerated aging behavior occurred. The deviation within the manipulated cells is large, as cell Man 3 degraded faster than the other two. The cell Man 2 degrades more strongly from cycle 300, and from cycle 600, all three manipulated cells had a significant drop in available discharge capacity. In the end of the cycle life testing at cycle 1002, the mean discharge capacity in the checkup of all manipulated cells was approximately 35% SOH. Also in the voltage curves, it can be observed that the manipulated cells aged faster. Already by cycle 202, the manipulated cells exhibited higher overpotentials in the charge curves, which led to reaching the maximum voltage limit more quickly. The same trend is evident in the discharge curves, where less capacity could be extracted due to increasing ohmic

resistance. Additionally, it is noticeable that the CV phase steadily increased during the life cycle testing within the checkup cycles in the manipulated cells. The introduction of excessively loaded cathodes into batch 2 provoked an intensified aging behavior of the battery cells. The faster aging behavior of the manipulated cells can be explained as follows: To the best of the authors knowledge, there is no conclusive literature on discussing the influence of differently heavily loaded electrode sheets in a cell stack. Therefore, a comparison is made with the parallel connection of battery cells in a module. All cathode sheets as well as anode sheets were interconnected through the cell's internal contacting, thus connected in parallel.^[48] The current, which was applied through the cell tester, was distributed to the individual electrode layers. However, the exact current density between the layers could not be precisely determined due to the varying loading. The differently loaded electrodes were at different degrees state of charges (SOC)^[49] and thus had different electrical resistances. Thus, the current will distribute inhomogeneously between the layers.^[50] Consequently, the electrodes were not cycled with 1 C, but with higher local C-rates, resulting in accelerated aging behavior of the electrodes.^[51,52]

Regarding the manipulated cells, this meant that the anodes opposite to the C3 cathode initially experienced accelerated aging due to overbalancing. This explained the significant initial drop in SOH within the first 50 cycles. As a result of local aging, the internal resistance of these electrode pairs increased, leading to an increasing distribution of current to other layers. This redistribution ensured that the remaining electrodes also aged due to higher current flow, which could have accounted for the second significant drop in SOH. In summary, the manipulation with an excessively loaded electrode sheet led to intensified aging at the cell level. Explaining the aging mechanism resulting from the more heavily loaded electrode

requires more extensive investigations. The exact current distribution between the electrode layers as well as the different SOCs of the individual electrode pairings must be investigated. However, this exceeded the scope of this work. The aim of this work was to demonstrate that an electrode-sheet-based traceability system can determine local electrode balancing. Since the N/P ratio has a crucial influence on cell cycling, the effects of unintended balancing could be demonstrated using the manipulated cells.

After the life cycle testing of 1002 cycles, a post-mortem analysis of the reference cells and the manipulated cells was performed. Figure 9 shows the opened cells Ref. [1] and Man 1. For the direct comparison of identical electrodes form the two cell batches, exemplary anodes A1, A2, A3, and the cathode C1 are shown in Figure 9a. To directly compare the anodes opposite the cathodes C3, they are shown enlarged in Figure 9b.

It can be observed that the anodes of the reference cells in Figure 9a, in comparison to the anodes of the manipulated cells exhibited a more homogeneous and clearer surface. All anodes of the manipulated cells showed flaky, silver contours, suggesting significant lithium plating.^[38,53–55] The anodes of the reference cells also exhibited small silver-colored traces, which may also indicate lithium plating. However, previous studies confirmed that even under normal operation conditions, lithium plating can occur due to cell cycling and aging.^[56] Furthermore, the separator of the reference cells was easily detachable from the surface of the anodes during cell opening and was much cleaner compared to the manipulated cells. Only minimal traces of anode particles were visible. In contrast, the separator of the manipulated cells exhibited an adhesive connection with the anodes upon opening and was significantly more contaminated after delamination, shown in Figure 9a below. Similar observations were made that active material is sticking to the separator

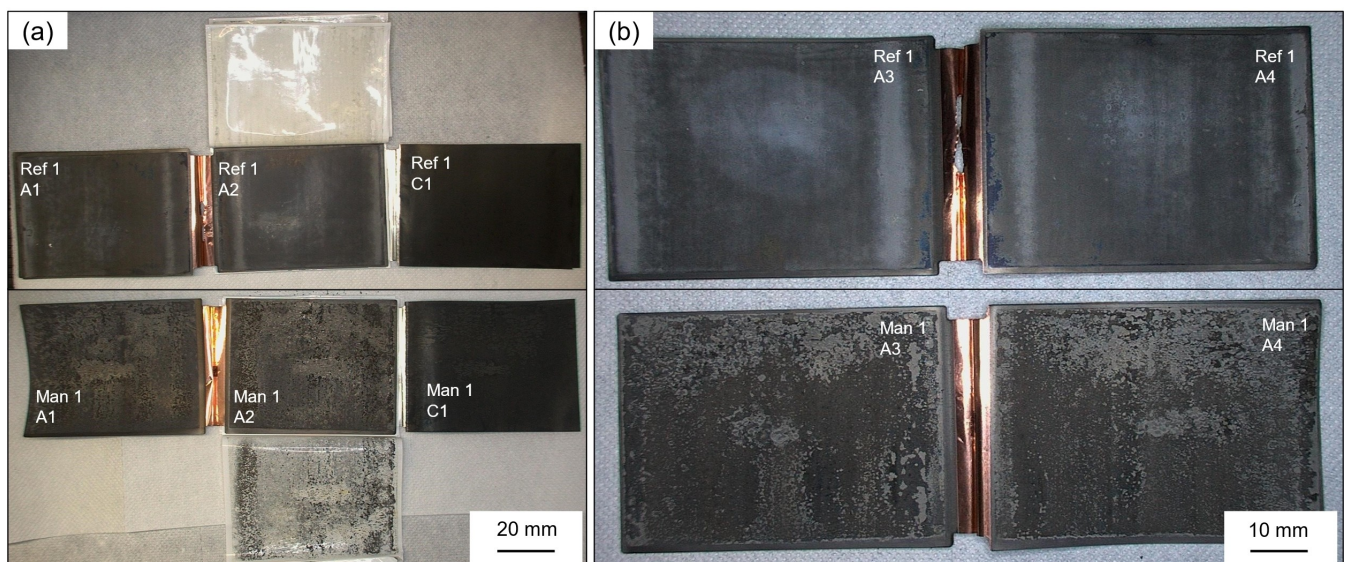


Figure 9. Post-mortem analysis of cell Ref. [1] and Man 1. In (a) the direct comparison of identical electrodes in both cell batches is shown. In (b) the anodes opposite to the C3 cathodes are shown in direct comparison between the Ref. [1] and Man 1 cells. The anodes of the manipulated cells exhibited in intensified visible lithium plating compared to the reference cells.

when lithium plating occurred,^[57] leading to the problems in separating the components.^[58] Figure 9b provides a direct comparison of the anode positions A3 and A4, in which the enhanced aging of the manipulated cells can be observed again. Despite the overloaded cathode C3 placed between the two anodes, all anode sheets of the manipulated cells display an identical visual appearance.

For a more detailed examination of the electrodes' surfaces, SEM images of the anodes from the reference and manipulated cells were taken. In Figure 10, lateral images of the cut edges as well as images of the surface of the electrodes are shown.

In Figure 10a, the anode sample of the reference cell is shown. It can be seen that the surface of the anode from the reference cells only shows minimal traces of lithium plating, which is identifiable by the white crystalline structures. In contrast, the anode of the manipulated cells is shown in Figure 10b. The surface section shows a boundary layer on the graphite particles and formed sediments. The deposited lithium appears in a frequently described mossy-like structure.^[59–61] The manipulated cells exhibited a significantly stronger lithium plating, as the surface of the electrode is covered with many white dendrites. This is evident both in the side and top views of the electrode. In summary, the introduction of the excessively loaded electrode sheet probably resulted in an uneven current distribution of individual electrode sheets, leading to accelerated aging of the manipulated cells.^[56] The images of the markings on the individual cathode and anode sheets are displayed in Figure 11.

It can be observed that the applied DMCs are still visible after cell opening. Using a handheld scanner (DS3608, Zebra Technologies Corp., USA), the contents or electrode IDs of the DMCs were scanned and read successfully. This was possible because the markings were not placed within the joining zone of the individual electrode sheets. In principle, the DMCs are not needed for the unique identification of the electrode sheets after the cell assembly since the information about the position of the electrode sheet and the orientation in the cell stack is

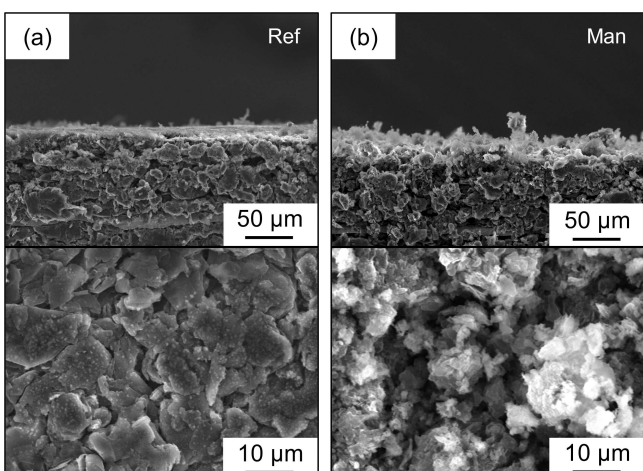


Figure 10. SEM images of the anodes of the reference cells in (a) and of the manipulated cells in (b). The side view of the cut-out sample is shown at the top and the surface images are shown at the bottom.

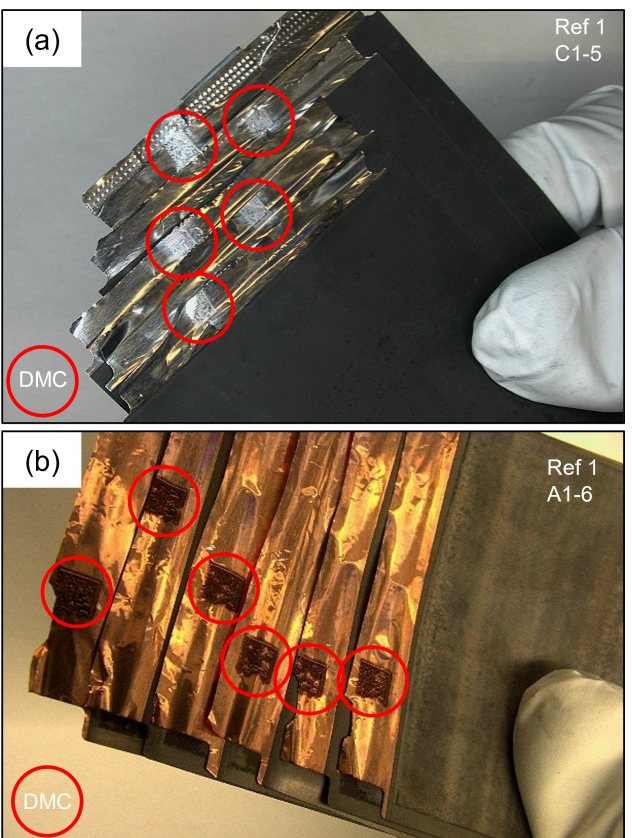


Figure 11. Images of the laser applied DMCs after the cell opening of all installed cathodes in (a) and all anodes in (b) of cell Ref. [1]. The codes remained readable after cell opening and could be used for tracking individual electrodes.

stored in the traceability system. Using the cell ID, each electrode sheet can be traced. Subsequently, production data associated with the electrodes can be extracted from the database. It is also noticeable that the DMCs have different positions on the collector flags. This is because the electrode confectioning was done manually, and not all electrodes had the exact same distance chosen.

Conclusions

The aim of this work was to demonstrate that a traceability system in battery cell production was used to determine the electrode balancing in multi-layer pouch cells. This approach can be used to detect production deviations and, consequently, establish quality gates. Using the produced pouch cells and the concurrently running traceability system, the areal mass loading was demonstrated as an example where production data was assigned specifically to each electrode sheet. In combination with the tracked stacking order, this data was used to form virtual representations of the cell stacks. By tracing the areal mass loading values of individual electrode sides, the opposing electrode sheets in the cell stack were identified, and the corresponding N/P ratio was calculated. It became evident from the cells that error-prone electrode sheets had entered the

production, altered the local N/P ratio, and caused accelerated aging. The manually introduced cathode sheet with extensive areal mass loading caused local lithium plating due to the overbalancing at the opposing anodes. This led to an increased capacity loss of the battery cell during cycling. By using a single electrode sheet that was outside the permissible tolerance regarding loading, the entire battery cell became qualitatively inferior as it exhibited a faster degradation behavior. The study proved that the N/P ratio has a crucial influence on the cell performance. Therefore, the traceability system with electrode sheet-specific data allocation allowed a deeper insight into the cell stacks and the corresponding electrode balancing. With this analysis, a pre-sorting of the electrodes after separation could have taken place to remove the defective intermediate products.^[62] This approach did not provide an exact prediction of the detailed progression of accelerated aging, a generally faster aging process could be predicted with high probability. Furthermore, it was already known after the coating process that these overly loaded electrode sheets did not comply with the specified tolerances. Post-mortem analysis provided additional explanations for the accelerated aging. It was also shown that the electrode IDs in the DMCs were still readable after cycling and available for traceability applications. Moreover, the use of a traceability system enables innovative analyses. Sensitivity analyses for coating data can be conducted using electrode-specific production data. For instance, by correlating targeted tolerance ranges with deviations of battery cells in cell testing, permissible limits or quality gates for each process step can be determined. In the context of this publication, fluctuations in the areal mass loading within a cell stack were correlated and quantified with cycle stability.

Acknowledgements

We express our gratitude towards the Federal Ministry of Education and Research (BMBF) for funding the research. The presented content in this paper has been achieved within the scope of the project "TrackBatt" (FKZ: 03XP0310A). Furthermore, we would like to thank our research partners and project coordinator Juelich for their trustful cooperation and support within the project. Further thanks are due to Filip Dorau, Johannes Lindenblatt, Matthias Leeb, Andreas Mayr, Alena Gründl, Sandro Stock, and Jan Hagemeister for their support in carrying out the cell production. We would also like to thank Johannes Schachtl for his support of the SEM images. Open Access funding enabled and organized by Projekt DEAL.

Conflict of Interests

The authors declare no conflict of interest.

Data Availability Statement

The data that support the findings of this study are available from the corresponding author upon reasonable request.

Keywords: lithium-ion battery production • tracking and tracing • electrode balancing

- [1] H. Lee, K. Calvin, D. Dasgupta, G. Krinner, A. Mukherji, P. W. Thorne, C. Trisos, J. Romero, P. Aldunce, K. Barrett et al., *IPCC, 2023, Climate Change 2023: Synthesis Report. Contribution of Working Groups I, II and III to the Sixth Assessment Report of the Intergovernmental Panel on Climate Change [Core Writing Team, H. Lee and J. Romero (eds.)]. IPCC, Geneva, Switzerland*, Intergovernmental Panel on Climate Change (IPCC), 202
- [2] L. Mauler, F. Duffner, J. Leker, *Appl. Energy* **2021**, 286, 116499.
- [3] F. Duffner, L. Mauler, M. Wentker, J. Leker, M. Winter, *International Journal of Production Economics* **2021**, 232, 107982.
- [4] Y. Liu, R. Zhang, J. Wang, Y. Wang, *iScience* **2021**, 24, 102332.
- [5] A. König, L. Nicoletti, D. Schröder, S. Wolff, A. Waclaw, M. Lienkamp, *WEVJ* **2021**, 12, 21.
- [6] A. Kwade, W. Haselrieder, R. Leithoff, A. Modlinger, F. Dietrich, K. Droeder, *Nat. Energy* **2018**, 3, 290–300.
- [7] R. Schmuck, R. Wagner, G. Hörpel, T. Placke, M. Winter, *Nat. Energy* **2018**, 3, 267–278.
- [8] M. F. Niri, K. Liu, G. Apachitei, L. R. Ramirez, M. Lain, D. Widanage, J. Marco, *J. Cleaner Prod.* **2021**, 324, 129272.
- [9] A. Turetskyy, J. Wessel, C. Herrmann, S. Thiede, *Energy Storage Mater.* **2021**, 38, 93–112.
- [10] F. M. Zanotto, D. Z. Dominguez, E. Ayerbe, I. Boyano, C. Burmeister, M. Duquesnoy, M. Eisentraeger, J. F. Montaño, A. Gallo-Bueno, L. Gold et al., *Batteries & Supercaps* **2022**, 5.
- [11] A. Turetskyy, S. Thiede, M. Thomitzek, N. von Drachenfels, T. Pape, C. Herrmann, *Energy Tech* **2020**, 8.
- [12] S. Thiede, A. Turetskyy, A. Kwade, S. Kara, C. Herrmann, *CIRP Ann.* **2019**, 68, 463–466.
- [13] S. Thiede, A. Turetskyy, T. Loellhoeffel, A. Kwade, S. Kara, C. Herrmann, *CIRP Ann.* **2020**, 69, 21–24.
- [14] J. Schnell, C. Nentwich, F. Endres, A. Kollenda, F. Distel, T. Knoche, G. Reinhart, *J. Power Sources* **2019**, 413, 360–366.
- [15] M.-A. Filz, S. Gelrlach, A. Turetskyy, J. Wessel, C. Herrmann, S. Thiede, *JMMP* **2020**, 4, 106.
- [16] J. Schnell, G. Reinhart, *Procedia CIRP* **2016**, 57, 568–573.
- [17] A. Turetskyy, J. Wessel, C. Herrmann, S. Thiede, *Procedia CIRP* **2020**, 93, 168–173.
- [18] J. Wessel, A. Turetskyy, O. Wojahn, C. Herrmann, S. Thiede, *Procedia CIRP* **2020**, 93, 162–167.
- [19] G. Rieixinger, J. P. Doppler, C. Haar, M. Trierweiler, A. Buss, K. Schöbel, D. Ensling, T. Bauernhansl, *Procedia CIRP* **2020**, 93, 125–130.
- [20] C. Connolly, *Assembly Automation* **2005**, 25, 182–187.
- [21] T. Pizzuti, G. Mirabelli, M. A. Sanz-Bobi, F. Goméz-González, *J. Food Eng.* **2014**, 120, 17–30.
- [22] R. Rotunno, V. Cesarotti, A. Bellman, V. Introna, M. Benedetti, *International Journal of Engineering Business Management* **2014**, 6, 25.
- [23] S. Stock, J. Hagemeister, S. Grabmann, J. Kriegler, J. Keilhofer, M. Ank, J. L. Dickmanns, M. Schreiber, F. Konwitschny, N. Wassiliadis et al., *Electrochim. Acta* **2023**, 471, 143341.
- [24] M. Ank, A. Sommer, K. Abo Gamra, J. Schöberl, M. Leeb, J. Schachtl, N. Streidel, S. Stock, M. Schreiber, P. Bilfinger et al., *J. Electrochem. Soc.* **2023** >.
- [25] A. Sommer, M. Leeb, S. Hagh, F. J. Günter, G. Reinhart, *Procedia CIRP* **2021**, 104, 1011–1016.
- [26] A. Sommer, M. Leeb, L. Weishaeupl, R. Daub, *Batteries* **2023**, 9, 89.
- [27] J. Wessel, A. Schoo, A. Kwade, C. Herrmann, *Energy Tech* **2023**, 11.
- [28] A. Schoo, R. Moschner, J. Hülsmann, A. Kwade, *Batteries* **2023**, 9, 111.
- [29] A. Sommer, S. Bazlen, H.-Y. Tran, W. Braunwarth, R. Daub, *Procedia CIRP* **2023**, 120, 171–176.
- [30] A. Sommer, S. Bazlen, H.-Y. Tran, M. Leeb, J. Wachter, W. Braunwarth, R. Daub, *Energy Tech* **2024**.
- [31] B. Son, M.-H. Ryoo, J. Choi, S.-H. Kim, J. M. Ko, Y. M. Lee, *J. Power Sources* **2013**, 243, 641–647.
- [32] R. Xue, H. Huang, G. Li, L. Chen, *J. Power Sources* **1995**, 55, 111–114.

- [33] M. F. Niri, G. Apachitei, M. Lain, M. Copley, J. Marco, *J. Power Sources* **2022**, *549*, 232124.
- [34] G. Reinhart, T. Zeilinger, J. Kurfer, M. Westermeier, C. Thiemann, M. Glonegger, M. Wunderer, C. Tammer, M. Schweier, M. Heinz in *Future Trends in Production Engineering* (Eds.: G. Schuh, R. Neugebauer, E. Uhlmann), Springer Berlin Heidelberg, Berlin, Heidelberg, **2013**, pp. 3–12.
- [35] D. Schreiner, T. Zünd, F. J. Günter, L. Kraft, B. Stumper, F. Linsenmann, M. Schüßler, R. Wilhelm, A. Jossen, G. Reinhart et al., *J. Electrochem. Soc.* **2021**, *168*, 30507.
- [36] J. Kriegler, L. Hille, S. Stock, L. Kraft, J. Hagemeister, J. B. Habedank, A. Jossen, M. F. Zaeh, *Appl. Energy* **2021**, *303*, 117693.
- [37] S. Stock, S. Pohlmann, F. J. Günter, L. Hille, J. Hagemeister, G. Reinhart, *J. Energy Storage* **2022**, *50*, 104144.
- [38] J. Hagemeister, S. Stock, M. Linke, M. Fischer, R. Drees, M. Kurrat, R. Daub, *Energy Tech* **2023**, *11*.
- [39] J. Kurfer, M. Westermeier, C. Tammer, G. Reinhart, *CIRP Ann.* **2012**, *61*, 1–4.
- [40] C.-S. Kim, K. M. Jeong, K. Kim, C.-W. Yi, *Electrochim. Acta* **2015**, *155*, 431–436.
- [41] B. F. Song, A. Dhanabalan, S. L. Biswal, *J. Energy Storage* **2020**, *28*, 101268.
- [42] F. J. Günter, N. Wassiliadis, *J. Electrochem. Soc.* **2022**, *169*, 30515.
- [43] C. D. Reynolds, P. R. Slater, S. D. Hare, M. J. Simmons, E. Kendrick, *Mater. Des.* **2021**, *209*, 109971.
- [44] M. Schmitt, M. Baunach, L. Wengeler, K. Peters, P. Junges, P. Scharfer, W. Schabel, *Chem. Eng. Process.* **2013**, *68*, 32–37.
- [45] J. Kasnatscheew, T. Placke, B. Streipert, S. Rothermel, R. Wagner, P. Meister, I. C. Laskovic, M. Winter, *J. Electrochem. Soc.* **2017**, *164*, A2479–A2486.
- [46] Y. Abe, S. Kumagai, *J. Energy Storage* **2018**, *19*, 96–102.
- [47] Z. Chen, L. Zhang, X. Wu, K. Song, B. Ren, T. Li, S. Zhang, *J. Power Sources* **2019**, *439*, 227056.
- [48] K. Tagawa*, R. J. Brodd in *Lithium-Ion Batteries* (Eds.: M. Yoshio, R. J. Brodd, A. Kozawa), Springer New York, New York, NY, **2009**, pp. 1–14.
- [49] W. F. Bentley in *The Twelfth Annual Battery Conference on Applications and Advances*, IEEE, **1997**, pp. 223–226.
- [50] A. R. Mandli, A. Kaushik, R. S. Patil, A. Nahá, K. S. Hariharan, S. M. Kolake, S. Han, W. Choi, *Int. J. Energy Res.* **2019**, *43*, 2044–2056.
- [51] Y. Gao, J. Jiang, C. Zhang, W. Zhang, Z. Ma, Y. Jiang, *J. Power Sources* **2017**, *356*, 103–114.
- [52] S. R. Sivakkumar, J. Y. Nerkar, A. G. Pandolfo, *Electrochim. Acta* **2010**, *55*, 3330–3335.
- [53] M. Ecker, P. Shafiei Sabet, D. U. Sauer, *Appl. Energy* **2017**, *206*, 934–946.
- [54] G. Zhang, X. Wei, G. Han, H. Dai, J. Zhu, X. Wang, X. Tang, J. Ye, *J. Power Sources* **2021**, *484*, 229312.
- [55] M. Petzl, M. A. Danzer, *J. Power Sources* **2014**, *254*, 80–87.
- [56] X. Lin, K. Khosravinia, X. Hu, J. Li, W. Lu, *Prog. Energy Combust. Sci.* **2021**, *87*, 100953.
- [57] T. Waldmann, S. Gorse, T. Samtleben, G. Schneider, V. Knoblauch, M. Wohlfahrt-Mehrens, *J. Electrochem. Soc.* **2014**, *161*, A1742–A1747.
- [58] T. Waldmann, A. Iturrondobeitia, M. Kasper, N. Ghanbari, F. Aguesse, E. Bekaert, L. Daniel, S. Genies, I. J. Gordon, M. W. Löble et al., *J. Electrochem. Soc.* **2016**, *163*, A2149–A2164.
- [59] L. Gireaud, S. Grugeon, S. Laruelle, B. Yrieix, J.-M. Tarascon, *Electrochim. Commun.* **2006**, *8*, 1639–1649.
- [60] Z. Li, J. Huang, B. Yann Liaw, V. Metzler, J. Zhang, *J. Power Sources* **2014**, *254*, 168–182.
- [61] J. Yamaki, S. Tobishima, K. Hayashi, K. Saito, Y. Nemoto, M. Arakawa, *J. Power Sources* **1998**, *74*, 219–227.
- [62] . Schmitt, A. Raatz, F. Dietrich, K. Dröder, J. Hesselbach, *CIRP Ann.* **2014**, *63*, 9–12.

Manuscript received: February 28, 2024

Revised manuscript received: April 13, 2024

Accepted manuscript online: April 23, 2024

Version of record online: June 7, 2024